Can area-wide building retrofitting affect the urban microclimate? An LES study for Berlin, Germany

Björn Maronga,[a,b] Matthias Winkler,[c] Dan Li,[d]

[a] *Leibniz University Hannover, Institute of Meteorology and Climatology, Herrenhäuser Straße 2, 30419 Hannover, Germany*

[b] *University of Bergen, Geophysical Institute, Norway*

[c] *Fraunhofer Institute for Building Physics IBP, Holzkirchen, Germany*

[d] *Department of Earth and Environment, Boston University, Boston, USA*

Corresponding author: Björn Maronga, maronga@muk.uni-hannover.de

ABSTRACT: In this work we investigate the effect of area-wide building retrofitting on summertime, street-level outdoor temperatures in an urban district in Berlin, Germany. We perform two building-resolving, week-long large-eddy simulations: one with non-retrofitted buildings and the other with retrofitted buildings in the entire domain to meet today's energy efficiency standards. The comparison of the two simulations reveals that the mean outdoor temperatures are higher with retrofitted buildings during daytime conditions. This behavior is caused by the much smaller inertia of the outermost roof/wall layer in the retrofitting case, which is thermally decoupled from the inner roof/wall layers by an insulation layer. As a result, the outermost layer heats up more rigorously during the daytime, leading to increased sensible heat fluxes into the atmosphere. During the nighttime, the outermost layer's temperature drops down faster, resulting in cooling of the atmosphere. However, as the simulation progresses the cooling effect becomes smaller and the warming effect becomes larger. After one week we find the mean temperatures to be 4 K higher during the daytime, while the cooling effects become negligible.

SIGNIFICANCE STATEMENT: Building retrofitting is taking place in Europe and other continents as a measure to reduce energy consumption. The change in the building envelope directly influences the urban atmosphere. Our study reveals that area-wide retrofitting in a German city district can have negative effects on the outdoor microclimate in summer by causing higher air temperatures.

1. Introduction

The world's urban population has been increasing for decades. In 2016, more than 54 % of the global population lived in cities and their surroundings (United Nations 2016). The most well-known consequence of urbanization is the air urban heat island (UHI), i.e., street-level air temperatures are generally found to be higher compared to rural environments. The UHI is most pronounced during nighttime and can be as high as 12 K (Oke et al. 2017), mainly because the absorbed solar radiation is stored inside building materials and pavements during the daytime and is released during the nighttime. Moreover, the longwave radiative cooling is limited due to the multiple reflection of radiation beams among buildings (i.e., radiation trapping), while the warming effect of anthropogenic heat flux is stronger at night. The daytime UHI is found to be much less pronounced because the rural areas are mostly open to solar irradiation and thus can heat up quickly in the morning hours. The urban environments are slower in heating up, sometimes resulting in morning urban cool islands (Theeuwes et al. 2015), but the stronger sensible heating in urban areas leads to similar air temperatures to those in rural areas in the late afternoon hours. In addition, the development of a convective boundary layer during the daytime allows the heat released from the surface to be rigorously mixed, both vertically and horizontally, and therewith diluting local surface differences.

In the context of climate change and UHI, urban heat mitigation has received growing attention (Krayenhoff et al. 2021). Different measures have been proposed to reduce temperatures in cities, such as green roofs and facades, reflective materials, implementation of blue infrastructures (lakes, flood detention basins), unsealing and renaturation of surfaces, and the optimization of newly-built up areas regarding cold air paths. A large number of previous studies have focused on quantifying the impacts of these measures in reducing urban temperatures and UHI intensities using numerical models (e.g. Li et al. 2014; Wang et al. 2020, 2021, among many others). Recently, Krayenhoff et al. (2021) gave a comprehensive review on modeling studies that focused on mitigation measures to avoid extreme heat in cities. Unfortunately, these measures are often not the priorities of cities' climate action plans, whose main aim is to reduce cities' energy consumptions and carbon emissions (Rosenzweig et al. 2010). Instead, building retrofitting is usually a high priority, especially for cities with many old buildings that have winter heating needs. Previous studies on building retrofitting have largely focused on its impacts on building energy efficiency (Rabani et al. 2017; Deb and Schlueter 2021) and indoor environmental quality (Ortiz et al. 2020). Cost-benefit analysis of building retrofit strategies often only considers the benefit from energy savings, which are relatiely easy to calculate (Asadi et al. 2012). However, the influence of building retrofitting on the outdoor microclimate has received almost no attention, which motivates the present work.

As retrofitting measures are implemented in the real world rather non-systematically and sporadically, it is nearly impossible to isolate the impact of building retrofitting on the urban atmosphere by means of in-situ measurements. Laboratory experiments (e.g. wind tunnel or test stand) often simplify many thermodynamical processes that are critical for addressing this problem or do not consider the full interactions between the building envelop and the urban atmosphere. Numerical modeling provides the ideal framework to perform scenario simulations with different building configurations. While large-scale weather and climate models coupled with so-called urban canopy models could, in theory, be used to tackle this problem, turbulent heat transfer in the bulk part of the urban canopy and heat transfer in the near-wall region (i.e., very close to solid surfaces where heat transfer is accomplished by molecular conduction) are parameterized in these models (Grimmond et al. 2010, 2011; Best and Grimmond 2015). These parameterizations are known to be deficient (e.g. Hagishima et al. 2005). Moreover, the flow around buildings is often not resolved in urban canopy models. In contrast, urban microscale models, which resolve the key dynamical (e.g., the flow around buildings) and scalar (e.g., turbulent heat) transfer processes in the urban atmosphere, have been increasingly used to study urban environmental issues (e.g. Letzel et al. 2008; Inagaki et al. 2011; Krayenhoff and Voogt 2007; Yaghoobian et al. 2014; Gronemeier et al. 2017; Sinsel et al. 2021, among many others), especially in the context of mitigating urban heat (e.g. Gross 2012; Ambrosini et al. 2014; Günther 2014; Gross 2017; Crank et al. 2018; Sinsel et al. 2021). However, to our best knowledge, using urban microscale models to quantify the effect of building retrofitting measures on the outdoor microclimate has not been attempted so far.

Most of the state-of-the-art urban microscale models used in the past research, such as MUKLIMO_3 (Früh et al. 2011), MITRAS (Schlünzen et al. 2003; Salim et al. 2018), ASMUS (Gross 2012), or ENVI-met (Bruse and Fleer 1998) are based on so-called Reynolds-Averaged Navier-Stokes (RANS) solvers, which parameterize the full spectrum of atmospheric turbulence. Large-Eddy Simulation (LES) models, on the other hand, resolve the large-scale turbulent eddies that are responsible for most of the momentum and scalar transfer. Although the near-wall region may still need to parameterized, the LES models have been shown to provide much more reliable results than RANS models for flows in the urban canopy layer and the atmospheric boundary layer flows in general (Letzel et al. 2008; Blocken 2018; Gronemeier et al. 2021). In the present work, we will employ the PALM model system in LES mode (Maronga et al. 2020), which has been continuously developed for applications in urban environments. For more details, please see the PALM 6.0 Special Issue 999 of *Geoscientific Model Development*[1].

The paper is organized as follows. Section 2 provides an overview of the PALM model, case description, and model-setup. Results are presented in Sect. 3. Section 4 gives a summary.

2. Model and case description

a. LES model

The PALM model system in revision 4856 was used for the present study. PALM solves the conservation equations for momentum, heat, and moisture in the Boussinesq-approximated form on a Cartesian staggered Arakawa–C grid. It has been widely used to study various aspects of the urban boundary layer (e.g. Letzel et al. 2012; Gronemeier et al. 2017; Resler et al. 2017; Kurrpa et al. 2020; Gronemeier and Sühring 2019). PALM allows to represent fully three-dimensional building topologies on the Cartesian grid. The size and the number of individual surface elements are defined through the grid spacings Δx, Δy, Δz in $x-$, $y-$, and $z-$direction of the Cartesian grid, respectively. Discretization in time was achieved by a third-order Runge–Kutta time-stepping scheme (Williamson 1980) and discretization in space was achieved by the default fifth-order advection scheme (Wicker and Skamarock 2002). Near solid walls the order of the advection scheme was successively degraded to have a smaller stencil. We used the 1.5-order subgrid closure after Deardorff (1980) in the formulation of Saiki et al. (2000), which solves an additional

[1]https://gmd.copernicus.org/articles/special_issue999.html

prognostic equation for the subgrid-scale turbulence kinetic energy. A full overview of PALM is given by Maronga et al. (2015, 2020).

For the present study, we used fully interactive surface models both for buildings (building surface model, BSM, Resler et al. 2017; Maronga et al. 2020) and for other natural and artificial surfaces (land surface model, LSM, Gehrke et al. 2021). Both components consist of an energy balance solver for the radiative temperature for each surface element, which is coupled to a multi-layer heat conduction model through the respective material attached to the surface (i.e. soil or pavement for the LSM component and window or wall for the BSM component). Note that PALM does not offer a full water model yet, so that the water temperature is a fixed parameter specified by the user. This should be acceptable for our study since temperatures of streaming water as present in our study do at most vary a few degrees in the diurnal cycle (and therefore one order of magnitude less than all other surface temperatures). In order to calculate the energy balance, BSM and LSM receive radiative fluxes from PALM's embedded Radiative Transfer Model (RTM, Salim et al. 2020; Krč et al. 2021), which is a fully 3-D model taking into account various surfaces and the plant canopy. The RTM is further coupled to the Rapid Radiative Transfer Model for Global Models (Clough et al. 2005, RRTMG), which is used to provide the radiative fluxes at the top of the urban canopy layer to the RTM. Physical parameters representing the properties of different soil types, vegetation canopies, or pavements are implemented as look-up tables in PALM. Details are given by Heldens et al. (2020) and Gehrke et al. (2021). Likewise, an extensive database provides physical properties for each individual building based on their usage (residential, non-residential) and year of construction. For validation of BSM and LSM, see Resler et al. (2017, 2021) and Gehrke et al. (2021), respectively.

The indoor environment was simulated using a holistic building model, which is integrated into the BSM and relies on the database that is employed by the BSM as mentioned earlier. The indoor model predicts the operative room temperature as well as the waste heat flux (in case air conditioning systems, hereafter referred to as A/C systems, are used). The latter is transferred back into the atmosphere. Currently, this waste heat is distributed equally over all surface elements of each story of each building as positions of A/C systems are usually unknown. Details of the indoor model are given by Pfafferott et al. (2021).

b. Case description and model set-up

In the present case study we focus on an area of about $2\,\text{km} \times 2\,\text{km}$ around the town square Ernst-Reuter-Platz in the city district Charlottenburg in Berlin, Germany (see Fig. 1). The area is located in the center of Berlin, whose size is of about $900\,\text{km}^2$. Berlin is situated in the East of Germany, about 150 km south of the Baltic Sea. The climate is generally oceanic, but with some continental influences. The summertime temperatures are moderately warm, but can be sometimes hot. As the region is relatively flat (particularly the chosen area), we neglected the differences in terrain height. The building configuration in the chosen domain is typical for central European cities. Based on municipal data the area was roughly partitioned into residential buildings (the southwestern part of the area) and non-residential buildings (hereafter simply referred to as office buildings, see Fig. 2a). Figure 2b shows that building heights are typically in the order of 20-30 m, with a small fraction of higher buildings. The highest building, located in the southeast of the area, has a height of 120 m. Furthermore, the area contains a significant amount of green surfaces like parks, vegetated backyards, numerous street trees, as well as parts of the river Spree and the Landwehr Canal (see Fig. 1 and Fig. 2c). Data for building heights as well as information about green elements were determined from openly available municipally data sources. Pavement types of the streets were inferred from OpenStreetMaps[2] and were classified to be mostly asphalt, sett pavers, or paving stones. In the present work we will focus on an idealized case and hence the data quality and correctness are not a primary concern. For details on the data sources used and data processing involved, the readers are referred to Heldens et al. (2020).

The model was discretized in space using $1024 \times 1024 \times 256$ grid points ($x \times y \times z$). The horizontal grid spacing was 2 m and thus fine enough to resolve the buildings and street canyons in the domain (see Fig. 2). In the vertical direction, a grid spacing of 2 m was used up to 150 m, above which a grid stretching was applied using a factor of 1.08 until a maximum value of 25 m was reached. We imposed a geostrophic wind speed of $1\,\text{m s}^{-1}$, blowing from the west and representing weak-wind conditions. The model was initialized by mean profiles of potential temperature and water vapor mixing ratio as shown in Fig. 3. The initial potential temperature profile was constant (293.15 K) up to a height of 1400 m, with a capping inversion of 1 K per 100 m above. The initial water vapor

[2]https://planet.openstreetmap.org/, last accessed: June 02, 2021

FIG. 1. 3-D map of the area around Ernst-Reuter-Platz, Berlin, Germany. Imagery ©Google, Imagery ©GeoBasis-DE/BKG, Geocontent, Maxar Technologies Map data ©GeoBasis-DE-BKG(©2009).

mixing ratio profile was a constant value of 5 g kg^{-1} below 1400 m, linearly decreasing over 100 m to 1 g kg^{-1} in the free atmosphere (i.e., above 1500 m).

In order to systematically analyze the effect of building retrofitting on the urban microclimate conditions we decided to run the model for seven consecutive summer days starting with 01 July 2019, 0000 UTC. However, to avoid trends imposed by varying incoming solar radiation due to the seasonal cycle, we reset the solar position after each 24 h of simulation time. In this way, we simulated one full week with the same radiative forcing each day. Furthermore, we used cyclic lateral boundaries, i.e., the simulated domain of 4 km^2 virtually repeated endlessly in the simulation. While this set-up had the advantage of avoiding the complexities associated with specifying an incoming flow, we prohibited fresh or cold air supply from areas outside the domain

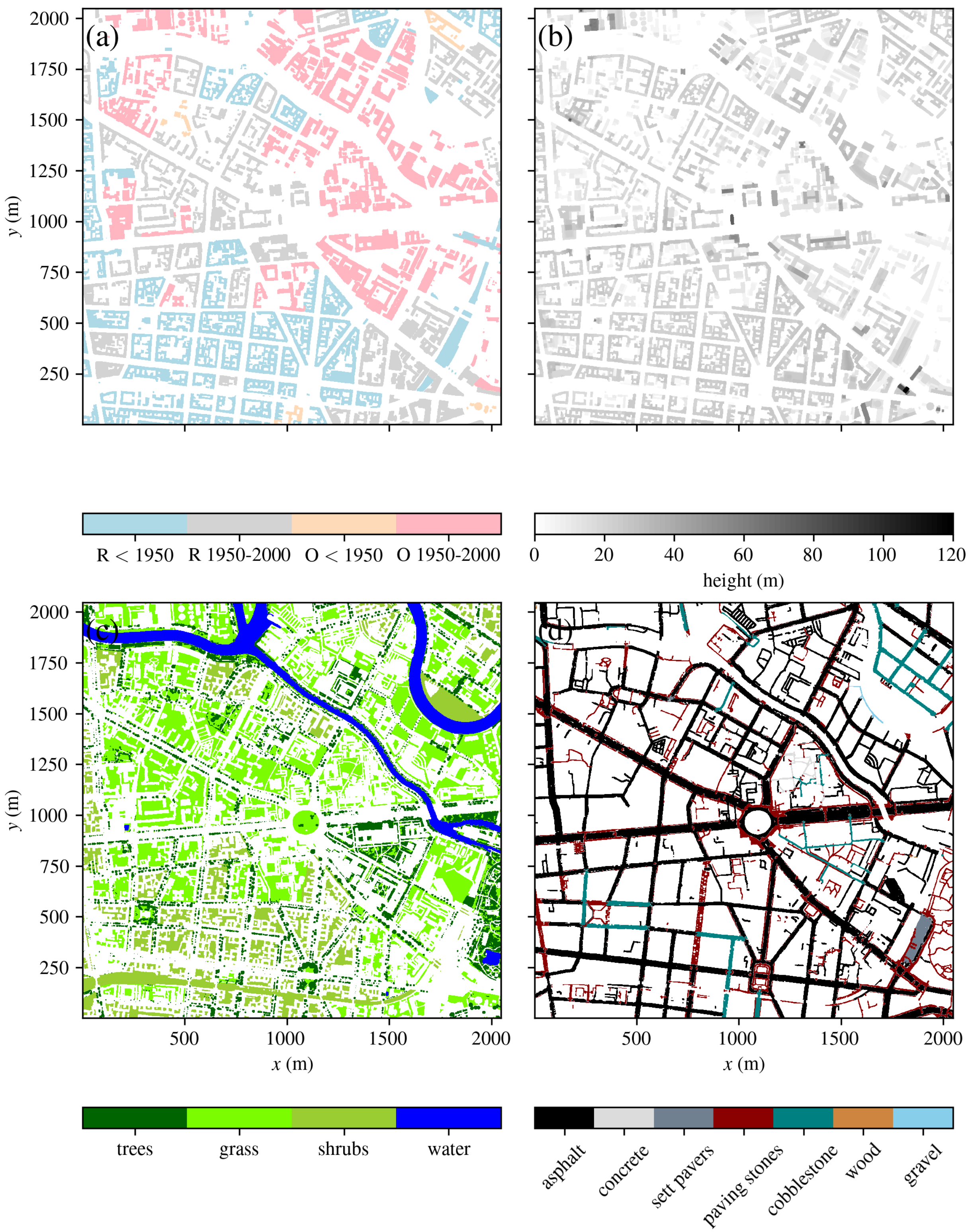

FIG. 2. Map of the building type classification in the simulation domain according to building use (R: residential, O: office) and year of construction, (b) building heights, (c) vegetation and water, and (d) pavement types in the simulation domain.

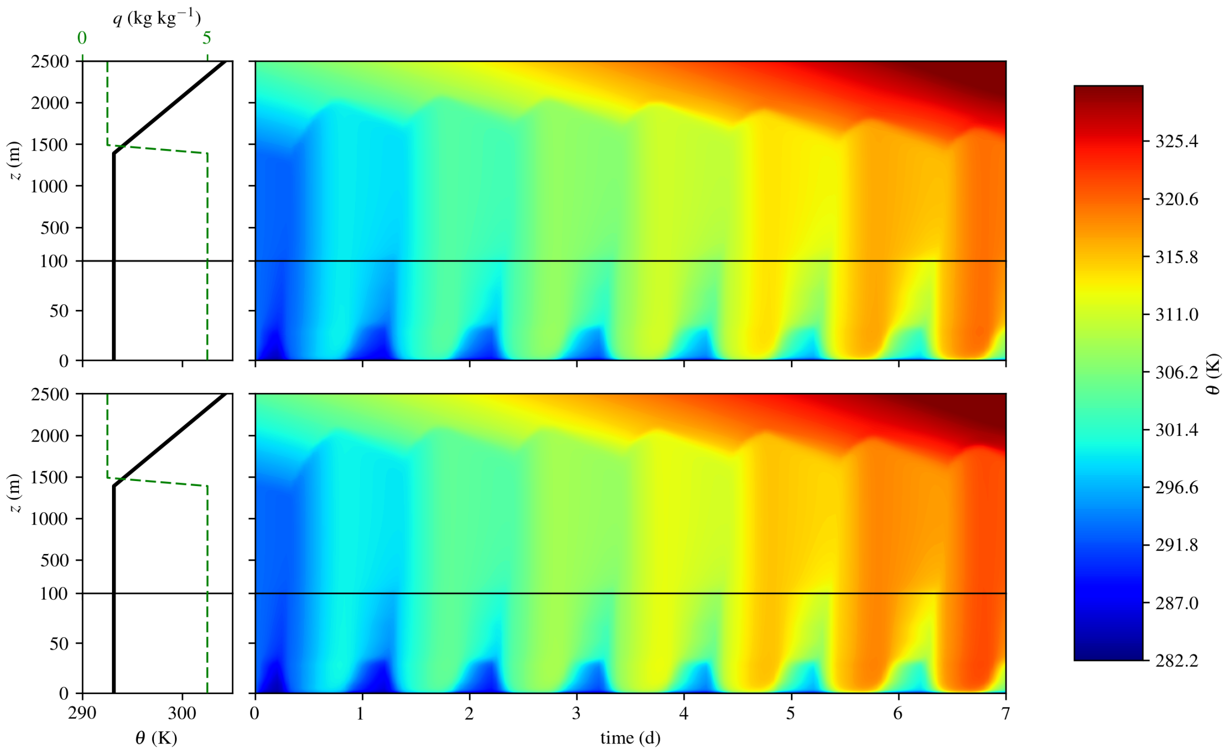

FIG. 3. Time-height plot of $\langle\theta\rangle$ for the baseline run (upper panel) and the retrofitting scenario (lower panel). Note that data for $z \leq 100$ m is displayed with a stretched vertical axis for better visibility. The change of the z−axis scaling is indicated by the black horizontal line. Initial profiles of $\langle\theta\rangle$ and $\langle q\rangle$ are additionally given in the left panels.

(e.g. the large Tiergarten park located nearby in the east of the domain). As this set-up would have led to a massive increase in the boundary-layer height over the simulation time, which would compromise the chosen horizontal domain size, we applied a large-scale subsidence velocity to counteract this increase. The subsidence velocity here was set to be 0.5 cm s^{-1} from the model top to the temperature inversion at a height of 1400 m, then linearly decreasing to zero at the surface. The subsidence was kept constant during the whole simulation period, mimicking conditions of a high pressure system, which is typical under heat wave conditions. Furthermore, we applied a Rayleigh damping starting at a height of 2000 m to prevent gravity waves from being reflected by the model top boundary.

The LSM was initialized using soil temperature and soil moisture content values as shown in Tab. 1, reflecting a relatively warm soil with enough water content to allow transpiration of plants.

TABLE 1. Initial soil temperature T_{soil}, volumetric moisture content m_{soil}, saturation moisture m_{sat}, field capacity m_{fc}, and wilting point m_{wilt} for the individual soil layers with thickness Δ_{soil}

Δ_{soil} (m)	T_{soil} (K)	m_{soil} ($\mathrm{m^3\,m^{-3}}$)	m_{sat} ($\mathrm{m^3\,m^{-3}}$)	m_{fc} ($\mathrm{m^3\,m^{-3}}$)	m_{wilt} ($\mathrm{m^3\,m^{-3}}$)
0.01	293.15	0.3	0.430	0.383	0.133
0.02	292.00	0.3	0.430	0.383	0.133
0.04	291.00	0.3	0.430	0.383	0.133
0.06	290.00	0.3	0.430	0.383	0.133
0.14	290.00	0.3	0.430	0.383	0.133
0.26	286.00	0.3	0.430	0.383	0.133
0.54	281.00	0.3	0.430	0.383	0.133
1.86	281.00	0.3	0.430	0.383	0.133

The soil type was set to be *medium-fine* according to PALM's soil porosity classification (see Gehrke et al. 2021). The water temperature was fixed to a value of 283 K. The BSM was initialized with wall, roof, and window temperatures of 293.15 K (i.e. all materials are in equilibrium at model start). The radiation models (RRTMG and RTM) were called each 60 s.

c. Scenarios

We conducted two simulations that only differ in terms of building construction and technology. In the first run both BSM and the indoor model were set up based on the built-in building database and the building classification as shown in Fig. 2a, represented the status quo situation. Note that information on year of construction and building usage is only available on the city block scale. Detailed information about usage and retrofitting of individual buildings is generally not registered in Germany and thus unknown. For simplification we thus assume that none of the buildings have been modernized. PALM's building database (Pfafferott et al. 2021) is largely based on a typology for German residential buildings (Loga et al. 2015). The most relevant parameters of PALM's default building configuration are listed in Tab. 2. In the second run, we virtually retrofitted all buildings in the domain by changing the buildings database (see Fig. 2b). The building typology specifies common retrofitting measures and materials for different building types, and its so-called "forward-looking" modernization package was used as the basis for our study. We adjusted the insulation thicknesses as well as the characteristic values of windows to meet or exceed the requirements of the most recent federal subsidy program for energy-efficient buildings (BMWi

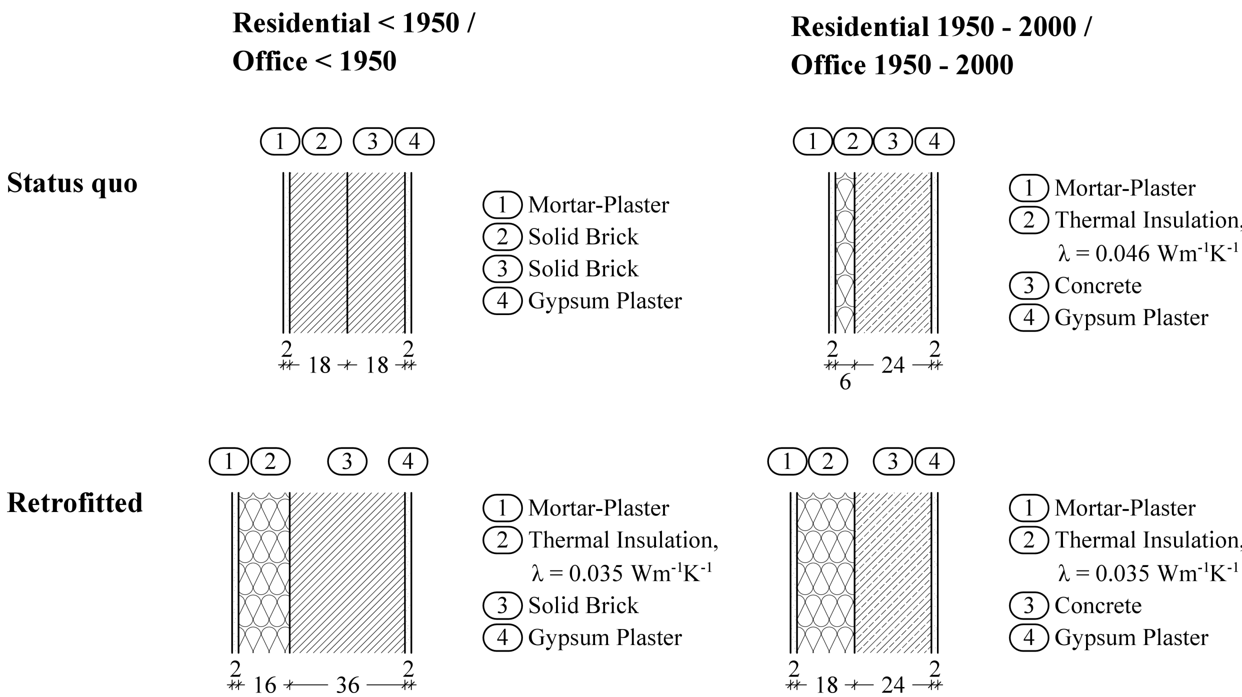

FIG. 4. Wall cross sections for the status quo and retrofitting scenarios. Thicknesses are given in centimeters

2021). The constructions were adapted to fit PALM's 4-layer surface model where necessary. As far as possible, the material data for retrofitting were taken from the existing PALM database or supplemented from standardized values from DIN 4108-4 (DIN 2020). Figs. 4 and 5 shows cross sections for the status quo and retrofitting scenarios for walls and roofs, respectively. Here we highlight the applied thermal insulation between the outer layer of plaster and the inner wall layers (roof tiles or bitumen and the inner roof construction layers) in the retrofitting scenario, as it plays an important role in determining the simulation results shown later. No adjustments were made to the floor slab constructions, as ground heat flow is currently not implemented in PALM's indoor model. A complete overview of the building envelope configuration including the material parameters in both the status quo and retrofitting cases is provided in Tab. A1 in the Appendix.

In the PALM building database, all buildings of the same age class have identical building constructions. This was also adopted for the retrofit measures, resulting in identical building envelope configurations for both residential and office buildings of the same age class. However, while the residential buildings did not have cooling in the retrofitting run, the plant technology for cooling in office buildings was adapted to efficient thermal component activation where cooling is activated once the indoor temperature exceeds 299.15 K. The heating system was not adjusted as the

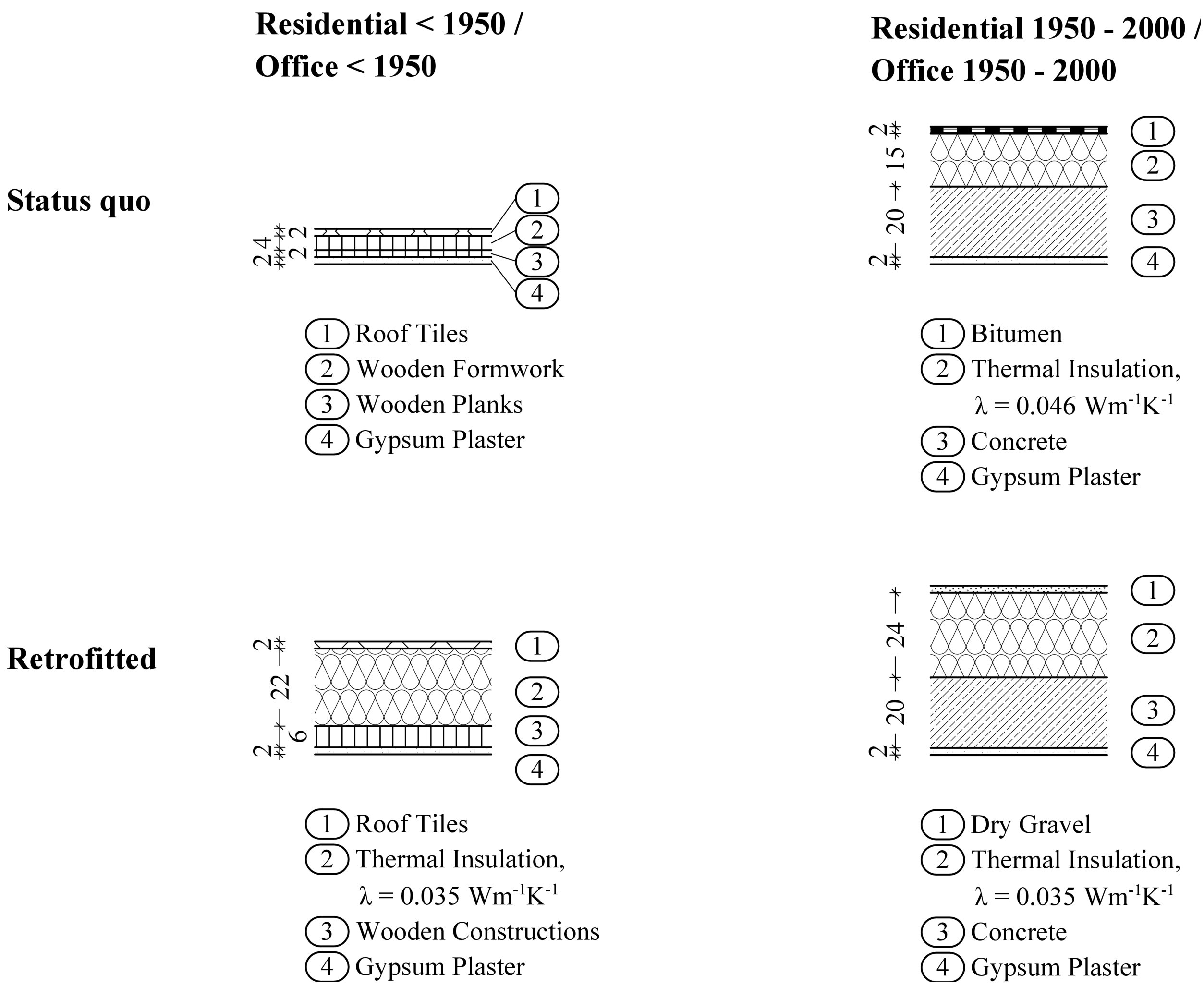

FIG. 5. Roof cross sections for the status quo and retrofitting scenarios. Thicknesses are given in centimeters

simulation was outside the heating period. The default values for utilization, internal loads, shading and ventilation stored in the PALM building database are based on standardized values from DIN 4108-2 (DIN 2013), a German standard for reducing summertime overheating in buildings. The key building parameters in the retrofitting run are summarized in Tab. 3.

3. Results

a. Indoor temperature

First of all, we examine the temporal evaluation of the indoor operative temperature (hereafter simply referred to as the indoor temperature) to assess whether the retrofitting measures have the expected impact on the indoor environment. That is, we expect the indoor temperature to

TABLE 2. Key building parameters used for the baseline (status quo) run

	Residential < 1950	Residential 1950 - 2000	Office < 1950	Office 1950 - 2000
Wall Construction	Solid brick masonry, $U = 1.57\,\mathrm{W\,m^{-2}\,K^{-1}}$	Concrete wall with thin external insulation, $U = 0.62\,\mathrm{W\,m^{-2}\,K^{-1}}$	Solid brick masonry, $U = 1.57\,\mathrm{W\,m^{-2}\,K^{-1}}$	Concrete wall with thin external insulation, $U = 0.62\,\mathrm{W\,m^{-2}\,K^{-1}}$
Roof Construction	Non-insulated wooden roof, $U = 1.41\,\mathrm{W\,m^{-2}\,K^{-1}}$	Concrete roof with thermal insulation, $U = 0.27\,\mathrm{W\,m^{-2}\,K^{-1}}$	Non-insulated wooden roof, $U = 1.41\,\mathrm{W\,m^{-2}\,K^{-1}}$	Concrete roof with thermal insulation, $U = 0.27\,\mathrm{W\,m^{-2}\,K^{-1}}$
Windows	Single glazing, $U_\mathrm{w} = 2.90\,\mathrm{W\,m^{-2}\,K^{-1}}$	Double glazing, $U_\mathrm{w} = 1.70\,\mathrm{W\,m^{-2}\,K^{-1}}$	Single glazing, $U_\mathrm{w} = 2.90\,\mathrm{W\,m^{-2}\,K^{-1}}$	Double glazing, $U_\mathrm{w} = 1.70\,\mathrm{W\,m^{-2}\,K^{-1}}$
Cooling System	No cooling	No cooling	No cooling	No cooling

TABLE 3. Key building parameters used for the run with retrofitted buildings

	Residential < 1950	Residential 1950 - 2000	Office < 1950	Office 1950 - 2000
Wall Construction	External wall insulation on solid brick masonry, $U = 0.19\,\mathrm{W\,m^{-2}\,K^{-1}}$	Concrete wall with thick external insulation, $U = 0.18\,\mathrm{W\,m^{-2}\,K^{-1}}$	External wall insulation on solid brick masonry, $U = 0.19\,\mathrm{W\,m^{-2}\,K^{-1}}$	Concrete wall with thick external insulation, $U = 0.18\,\mathrm{W\,m^{-2}\,K^{-1}}$
Roof Construction	Wooden roof with thermal insulation, $U = 0.14\,\mathrm{W\,m^{-2}\,K^{-1}}$	Concrete roof with thick thermal insulation, $U = 0.14\,\mathrm{W\,m^{-2}\,K^{-1}}$	Wooden roof with thermal insulation, $U = 0.14\,\mathrm{W\,m^{-2}\,K^{-1}}$	Concrete roof with thick thermal insulation, $U = 0.14\,\mathrm{W\,m^{-2}\,K^{-1}}$
Windows	Triple glazing, $U_\mathrm{w} = 0.80\,\mathrm{W\,m^{-2}\,K^{-1}}$	Triple glazing, $U_\mathrm{w} = 0.80\,\mathrm{W\,m^{-2}\,K^{-1}}$	Triple glazing, $U_\mathrm{w} = 0.80\,\mathrm{W\,m^{-2}\,K^{-1}}$	Triple glazing, $U_\mathrm{w} = 0.80\,\mathrm{W\,m^{-2}\,K^{-1}}$
Cooling System	No cooling	No cooling	Thermal component activation , Waste-heat-factor 1.25	Thermal component activation, Waste-heat-factor 1.25

show less warming in the retrofitting case due to the better insulation. Figure 6 shows the mean (domain-averaged), maximum, and minimum indoor temperatures for both simulations, and the differences between the retrofitting and baseline scenarios. Note that the variability here refers to horizontal variation only. The indoor temperatures were averaged over height in post-processing of the data. In both simulations the mean indoor temperature is increasing almost linearly with time, with values about 293 K at the beginning of the simulation and values about 295-300 K after one week. The minimum values follow the same linear trend, but display decreasing trends in some periods, possibly due to nocturnal ventilation through windows. The minimum values are usually observed in the ground story where direct solar irradiation is to a large extent absent in the diurnal cycle (not shown). The maximum temperatures, however, are considerably higher, with values up to 313-320 K, and display clear diurnal variations. These maximum values are reached in exposed buildings with high surface to volume ratios, which have high solar irradiation all day long (not shown). It is also visible that in the retrofitting scenario, the amplitude of the diurnal variations of the maximum temperatures is smaller due to the better insulation of the building envelope. The difference plot shows that the difference in the mean indoor temperature is also increasing roughly linearly in time and reaches -4 K after one week. The reduction of the mean indoor temperature in the retrofitting case is consistent with our expectation as alluded to earlier, and is the combined effect of improved building insulation and the operation of A/C systems in the office buildings. The differences in the maximum and minimum indoor temperatures reflect their respective behaviors as outlined above. It is noteworthy that the maximum temperature difference seems to run into a steady-state after three days and also displays clear diurnal variations, having its minimum of about -6 K in the evening hours and its maximum of -3 K shortly before noon. We can ascribe this diurnal cycle to the lag between the minimum and maximum values (of the timeseries of the maximum temperatures) caused by the discussed delay of heat transfer through the wall layers in the retrofitting scenario. These maximum values are found in residential buildings only as the office buildings are cooled to 299.15 K by A/C systems. In summary, we can conclude that the model produces the expected behavior of the indoor temperature and there is clear benefit of building retrofitting in mitigating extreme hot indoor conditions.

b. Boundary-layer development

Figure 3 shows a time-height diagram of the horizontally-averaged potential temperature $\langle\theta\rangle$ over the full simulation period for both cases. The diurnal cycle is well developed for the baseline run, with a convective boundary layer developing during daytime and a stable boundary layer during nighttime (visible by blueish colors near the surface). The bulk boundary-layer temperature increases in time due to a net heating from the surface over the diurnal cycles (shown and discussed later). The boundary-layer height during the first few days, indicated by a temperature jump across the interface between the mixed layer and the free atmosphere, reaches up to 2000 m during the daytime, while the nocturnal stable layer extends to heights of approximately 100 m. However, after about four days, we observe a slightly decreasing daytime boundary-layer height. After seven days the boundary-layer height reaches a height of 1600 m. This decrease is caused by the imposed large-scale subsidence in combination with the fact that the boundary layer itself is warming over time. The latter reduces the temperature gradient between the boundary layer and the surface. This

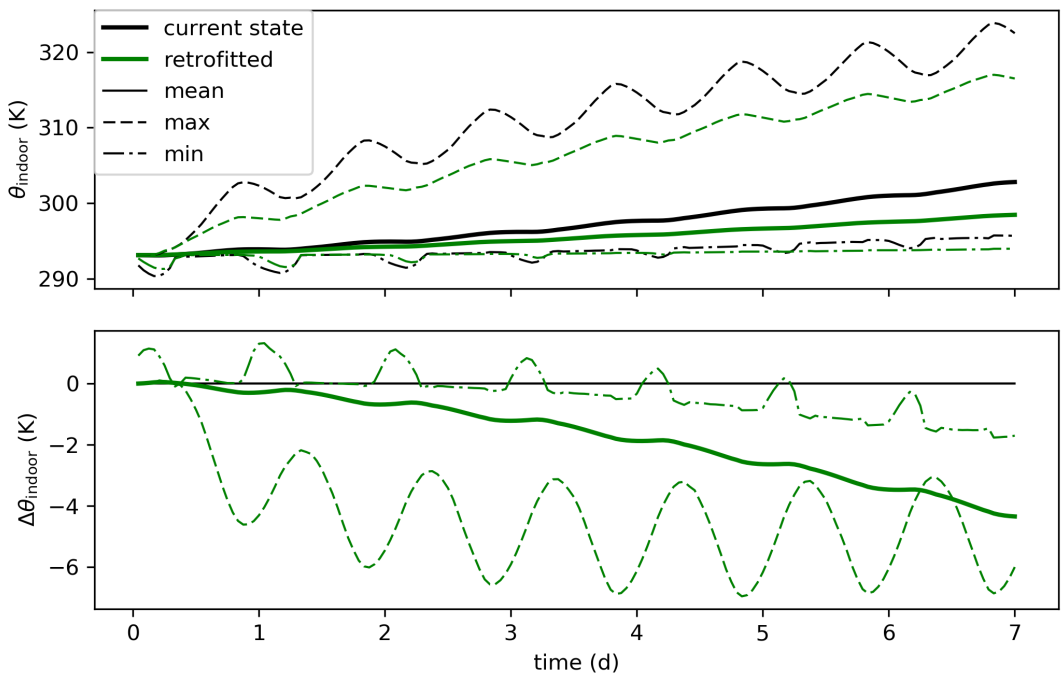

FIG. 6. Time series of the indoor temperature (upper panel) and the differences between the retrofitting and baseline runs (lower panel). Shown are mean (domain-averaged) values as well as maximum and minimum values. Note that indoor temperatures were averaged over each vertical column and thus the minimum and maximum temperatures indicate horizontal variations.

in turn leads to smaller sensible heat fluxes into the atmosphere (see Sect. d), resulting in a reduced boundary-layer growth over time.

Comparing the retrofitting scenario to the baseline scenario, Figure 3 reveals, one the one hand, that the boundary-layer temperatures become visibly higher in the retrofitting scenario. This becomes more pronounced towards the end of the simulation period. On the other hand, there is not much difference in the development of the nocturnal stable boundary layer. We also analyzed the differences in the boundary-layer height, but found only small differences between the retrofitting and baseline scenarios (not shown).

c. 2 m-temperature

We now assess the effect of area-wide building retrofitting on the outdoor temperatures. For this purpose we employ the 2 m-air potential temperature as it represents the layer where humans reside when they are outside the buildings. Grid cells occupied by buildings are excluded from the analysis. Figure 7 (top panel) shows the mean (domain-averaged) 2 m-temperature along with the maximum and minimum values found in the domain for both simulations. First of all, we see a clear diurnal cycle with minimum temperatures shortly before sunrise and maximum temperatures in the late afternoon. The simulations show a trend towards warmer temperatures (cf. Fig. 3). In the first diurnal cycle the mean temperature ranges from 285 K to 300 K in the baseline run, while on the last day, the mean temperature does not drop much below 300 K during the nighttime and reaches 318 K during the daytime. This strong trend is partly caused by the positive net heat input from the surface and the large-scale subsidence, but also partly because of the chosen periodic lateral boundary conditions, which "trap" the air inside the model domain. Warm air masses thus could not be advected out of the domain and be replaced by cold fresh air from other locations. As a consequence, the simulation suffers from overheating of the urban atmosphere over time. The maximum temperature follows the same diurnal cycle and trend as the mean value, but with an offset of about 10 K. In contrast, the diurnal cycle is considerably weaker for the minimum temperature, but it shows the same trend toward higher values in the course of time. Note that the minimum temperatures are usually observed close to the surface which are exposed to much less solar irradiation (see Sect. 3 a).

Figure 7 (bottom panel) also reveals the differences in the 2 m-temperature between the two scenarios. On the first night, we see a cooling effect (i.e., negative differences) for the retrofitting scenario starting roughly around midnight and increasing until just before sunrise (this coincides with the minimum temperature). On the second night, this cooling effect reaches its maximum magnitude of -1 K. In contrast, a warming effect of building retrofitting is evident during daytime, which is most pronounced in the late afternoon, coinciding with the maximum temperature. As time goes on, the positive differences are increasing in magnitude, while negative differences are decreasing in magnitude, resulting in a maximum warming of about 2.5 K during daytime and negligible cooling during nighttime after one week of simulation. This finding suggests that the net effect of building retrofitting on the street-level temperature is a positive one (i.e. warming)

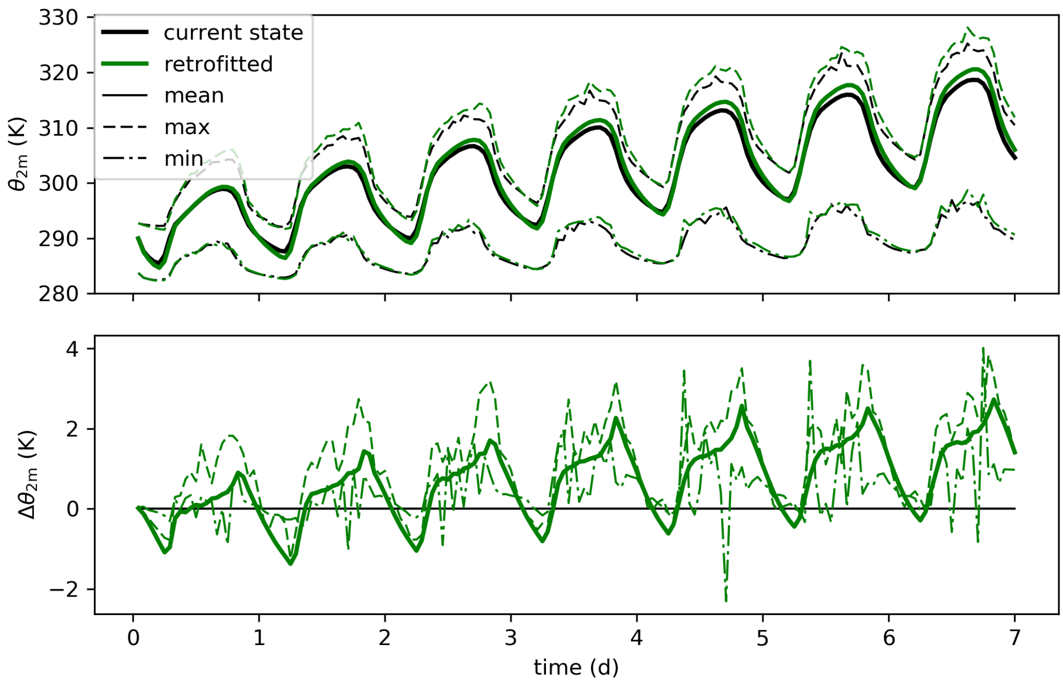

FIG. 7. Time series of the 2-m potential temperature (upper panel) and the difference between retrofitting scenario and baseline run (lower panel). Shown are mean (domain-averaged) values as well as maximum and minimum values.

and this warming effect becomes stronger for longer simulation periods. We will further discuss the cause for this behavior in Sect. 3 d.

Looking at the minimum and maximum values found in the difference between the baseline and retrofitting scenarios, it is clear that these must be controlled by fine features like turbulent fluctuations, radiation, and so on. No clear trend is visible, though the minimum and maximum values are also mostly positive during times where the mean value is positive and vice versa.

The spatial variability of the 2 m-temperature (averaged over 1 h) is shown for two snapshots (early morning, 0500 UTC; and late afternoon, 1600 UTC; they correspond to 0700 and 1800 local time, respectively) on the second day (Fig. 8) and on the last simulated day (Fig. 9) together with a difference plot between the baseline and retrofitting scenarios. The chosen times here coincide with the times of the day where we observed the largest magnitude of cooling and warming effects of building retrofitting. While on the second day we observe a clear cooling effect of retrofitting during the early morning and a warming effect during the late afternoon with realistic air temperatures, the last simulated day shows a small warming effect during the early morning and a significant warming effect during the late afternoon, and is characterized by unrealistically high air temperatures due to lack of fresh air supply.

In terms of the broad spatial patterns, both baseline and retrofitting scenarios display similar characteristics. For the early morning conditions (top panles), we find a heterogeneous temperature distribution in the domain, with relatively higher temperatures in the central and south-western part of the domain but lower temperatures close to the water patches (river Spree and Landwehr canal) and the less densely built-up area in the eastern part of the domain where there is a large amount of trees. The difference plot reveals a general cooling effect of retrofitting in the morning of the second day (up to 4 K). However, on the morning of the last day, a warming effect is observed in the central, northern, and eastern parts of the domain of up to 3 K. This pattern is linked directly to the building usage (see Fig. 2a): as the retrofitted office buildings are equipped with A/C systems, a significant amount of waste heat is released to the outdoor air, whereas the residential buildings do not have A/C systems installed (which is customary in Germany). The reason why we do not see this effect on the second day is that A/C systems were not active at that time (because both the indoor and outdoor environments were not warm enough). The fact that we still see a cooling effect in the south-western part of the domain on the last day suggests that the nocturnal cooling effect is generally stronger and lasts considerably longer in residential areas (i.e., in regions without A/C systems) during heat episodes.

In the late afternoon (bottom panels), both scenarios show high temperatures with maximum values around 304 K and 326 K on the second and last day, respectively. Only the water patches and the highly vegetated area in the east have lower temperatures. The values on the last day are probably too high for European cities, but can be explained by the cyclic lateral boundary conditions in combination with the imposed large-scale subsidence as already discussed. Since we are focusing on idealized conditions, this does not compromise the comparison of the two scenarios in terms of first-order effects, although it might have implications for heat transfer between the surface and the atmosphere on the later days of the simulation. The difference plots show a late afternoon warming effect as large as 4.5 K (second day) and 6 K (last day) due to building retrofitting. On close look we further find that the warming effect is most pronounced in narrow backyard areas,

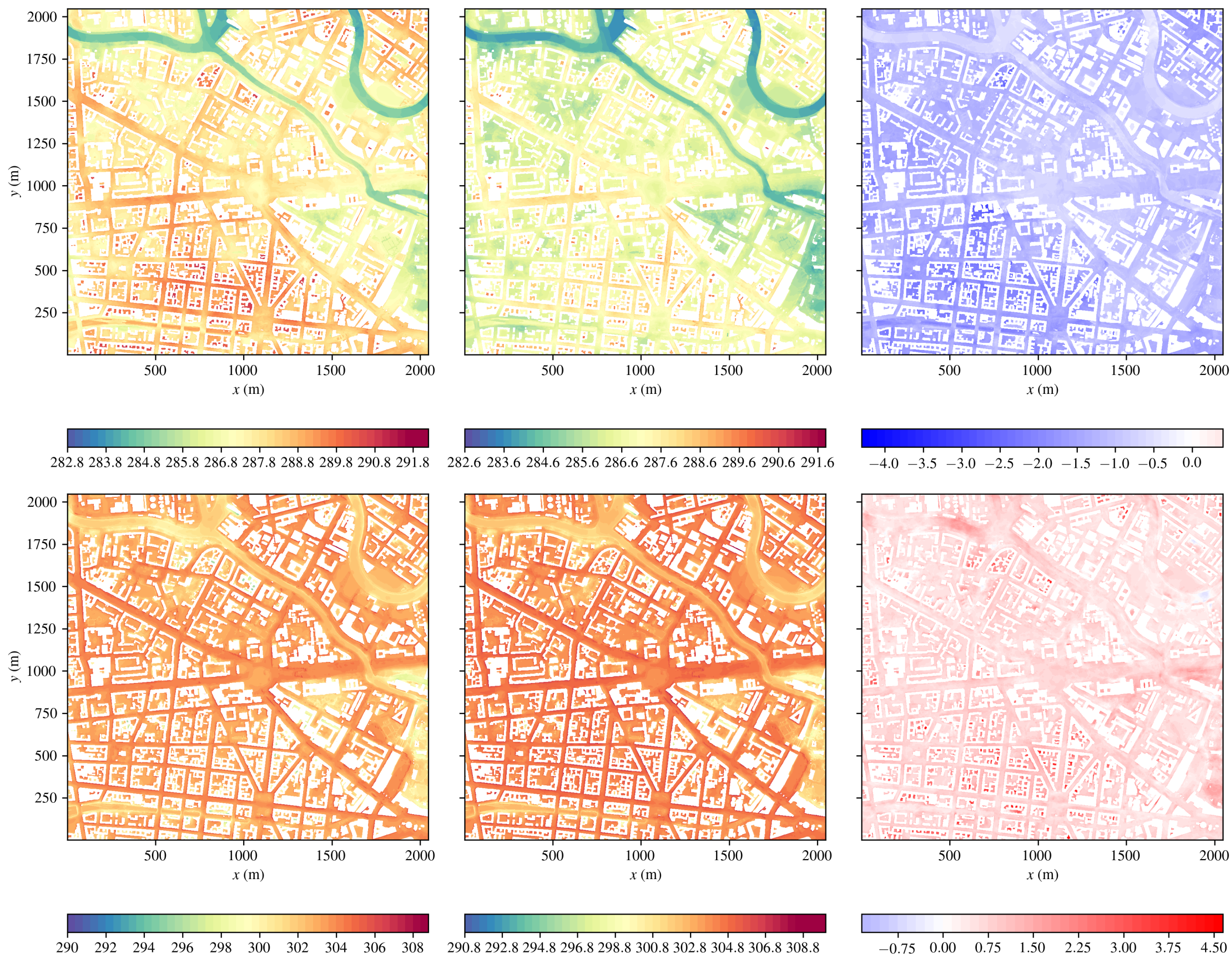

FIG. 8. Horizontal cross-sections of the 1 h-averaged 2 m-air potential temperature for (left panel) the baseline run, (middle panel) the retrofitting run, and (right panel) difference between the retrofitting and baseline runs on day two, i.e. after 29 h (0500 UTC, top panel) and after 40 h (1600 UTC, bottom panel).

i.e., over those areas which display the lowest air temperatures in the baseline scenario, and partly over the rivers. We hypothesize that this is a consequence of the excessive mixing in the retrofitting scenario so that persisting horizontal gradients during the daytime between relative cold air in the backyards and over the rivers become smaller. The relative heating over the colder areas is thus stronger than that over the warmer built regions.

In order to further understand how near-surface temperatures change due to retrofitting, Fig. 10 shows histograms of the 2 m-temperature as shown in Figs. 8 and 9. At 0500 UTC on the second day (top left panel), we see a shift of the multimodal distribution towards lower temperatures in the

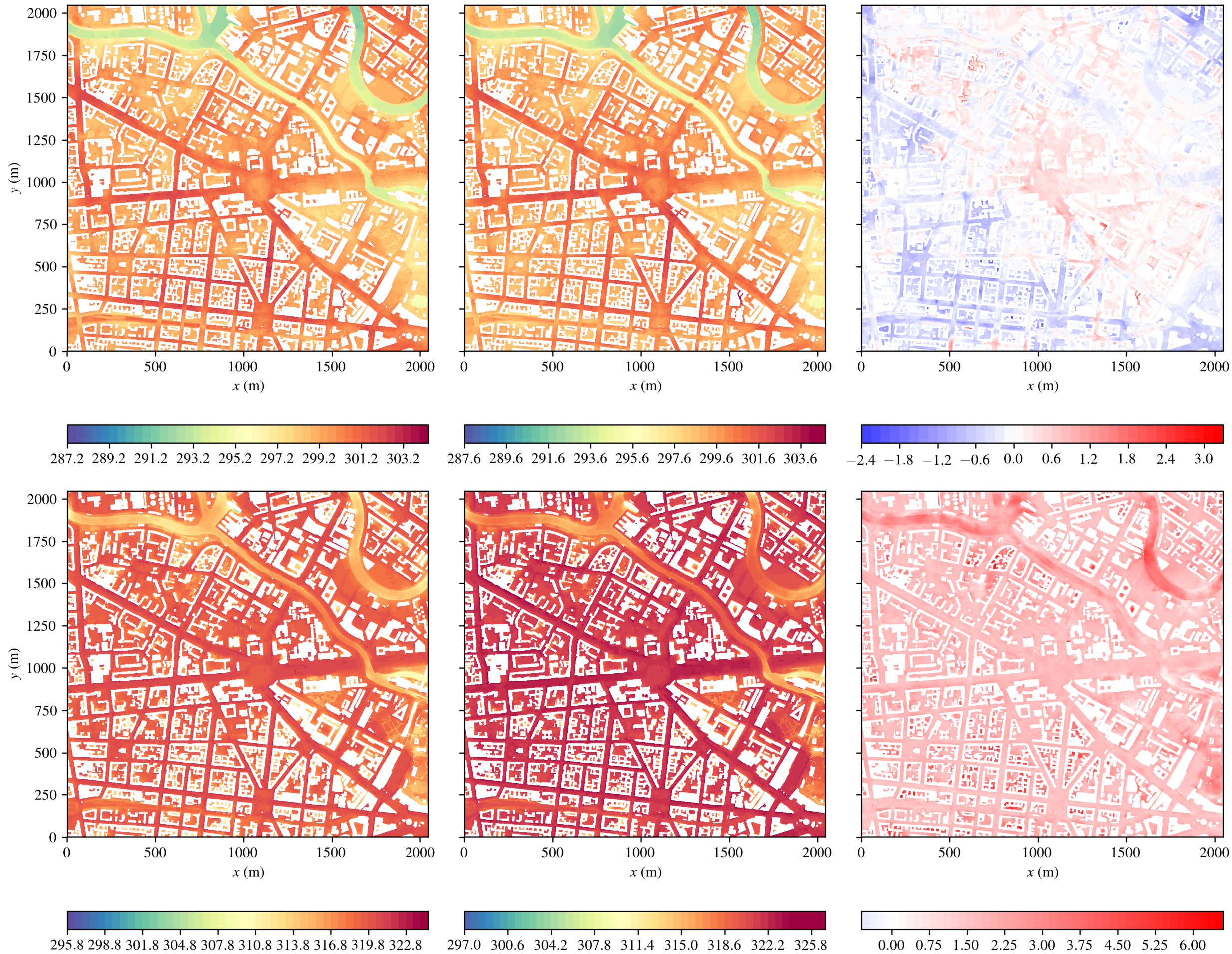

FIG. 9. As Fig. 8 but for the last simulated day i.e. after 149 h (0500 UTC, top panel) and after 160 h (1600 UTC, bottom panel).

retrofitting scenario. Here, the peak is found around 288 K in the baseline run and is reduced by 1.5 K in the retrofitting scenario. Furthermore, we observe a decrease of the second peak around 291 K and find that the third peak in the baseline run at 291 K has significantly reduced in the retrofitting case. For the last simulated day (bottom left panel), frequencies in bins with the highest temperatures (around 310 K) as well as around the 300 K-peak increase in the retrofitting scenario, while frequencies in the temperature range of 301-304 K decrease. Interestingly, we note almost no changes in the temperature range 290-297 K. Overall, these results suggest that building retrofitting affects the entire distribution of 2 m-temperature in the early morning.

For the late afternoon period, unimodal left-skewed distributions with the maximum frequencies in bins around 304 K (on the second day, top right panel) and 320 K (on the second day, bottom right panel) are observed in the baseline run. Building retrofitting results in shifts of the frequencies in all bins towards higher temperatures with peaks around 305 K and 322 K on the second and last day, respectively, amounting to an average shift of 1 K (second day) and 2 K (last day). That is, we observe no evident changes in the distribution for the late afternoon period. The different changes in the temperature distributions in the early morning and late afternoon periods can be explained by the different roles of turbulent mixing. During the night and early morning, turbulence is weak and turbulent eddies are relatively small. The propagation of perturbations induced by building retrofitting into the atmosphere is thus limited, which remain local and are strongly tied to the different building typologies and the presence of A/C system (only on the last days of the simulation). During the daytime, however, convection provides rigorous mixing of near-surface air with the entire boundary layer, so that any signal from changes in the surface conditions is diluted in the urban atmosphere. As a direct consequence, we see almost uniform temperature changes, except for locations near the water and highly vegetated areas (cf.. Figs. 8- 9).

d. Surface energy budget

In order to explain the differences in outdoor and indoor temperatures between the baseline and retrofitting scenarios, we analyze the energy budget at the surface, or the interface between the atmosphere and the sub-surface materials (and the indoor space). Figures 11 and 12 show the time series of the domain-averaged energy budget at the surface for horizontally-oriented surface elements treated by the the BSM (i.e., roofs) and the LSM (vegetation, bare soil, pavements, water), respectively. Note that we were not able to output and analyze all data for vertically-oriented building surfaces (walls and windows). The retrofitting measures for roofs were implemented similar to that for walls, i.e., by an additional thermal insulation layer covered by roof tiles (or bitumen) instead of the plaster used as outermost wall layer (see Fig. 5). The roof data can thus be used as a reasonable proxy for the behavior of the walls. By the same token roofs in the simulation domain are rarely affected by direct shadowing effects.

Analyzing the surface energy budget for roofs in the baseline run, we first note a clearly developed diurnal cycle, whose main characteristics does not change much over the simulation period, i.e.,

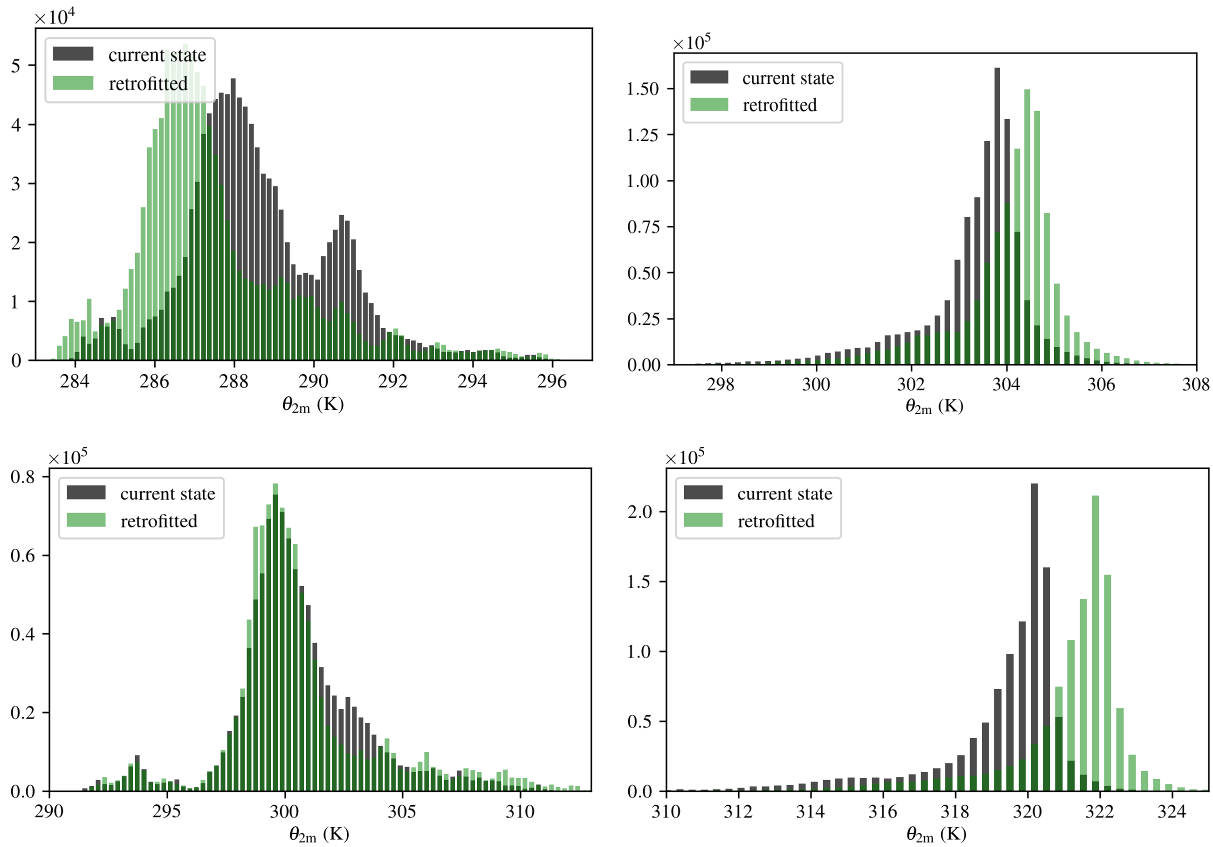

FIG. 10. Histograms of the 2-m potential temperature between retrofitting and baseline run on the second day after 29 h v(0500 UTC, top left panel) and 40 h (0500 UTC, top right panel) and on the last simulated day after 149 h (0500 UTC, bottom left panel) and 160 h (1600 UTC, bottom right panel

the surface energy budget appears to be in a quasi-steady state quickly after model start. We note a tendency of the sensible heat flux towards smaller fluxes over time, which is caused by the continuous increase of the air temperature, which reduces the temperature gradient between the surface and the near-surface air. During the daytime, the available energy at the surface (represented by the net radiation R_{n}) reaches values around $122-140\,\mathrm{W\ m^{-2}}$, which decreases to $-30\,\mathrm{W\ m^{-2}}$ during the nighttime. Note that the shown data are summed over all roof grid points and subsequently divided by the total number of horizontal grid points in the domain. As a consequence, the values appear much smaller than the ones found at a specific grid point. During the daytime this energy is partitioned into the sensible heat flux into the atmosphere of $H = 80-110\,\mathrm{W\ m^{-2}}$ and into the conductive heat flux into the building $G = 50-60\,\mathrm{W\ m^{-2}}$, while

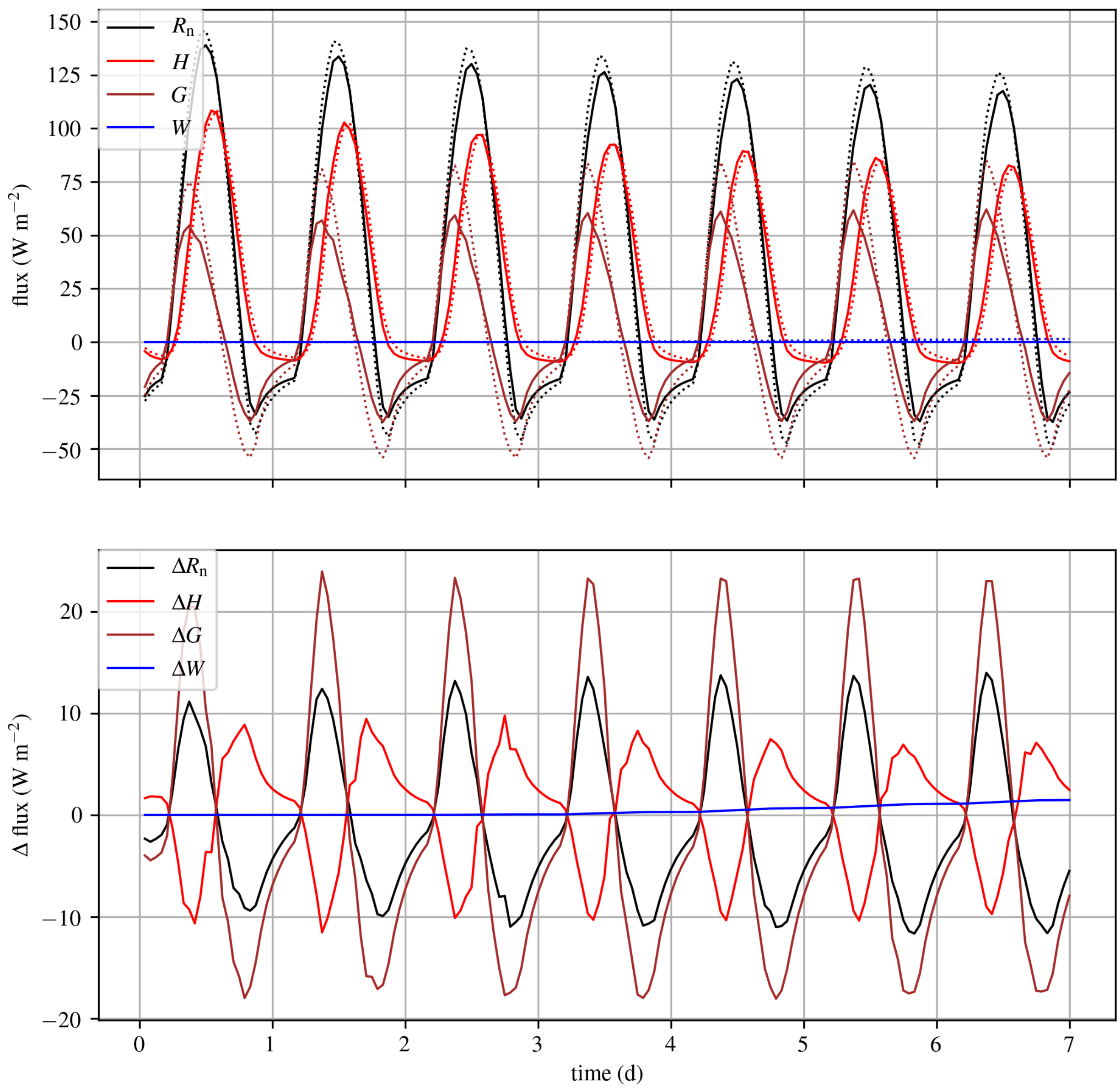

FIG. 11. Time series of the domain-averaged energy budget for both runs (top panel) and the change due to building retrofitting (bottom panel). Data from the baseline (current state) run are given as solid lines, while the retrofitting data is denoted as dashed lines. Only horizontally-oriented building surface pixels were summed up (i.e. only the roofs) and divided by the total number of horizontal grid points in the domain. Note that the net radiation R_n is defined positive downwards, while the surface flux of sensible heat H and the ground heat flux G are defined positive away from the surface. The latent heat flux is not shown as it was zero for two scenarios (no green roofs). The anthropogenic waste flux W from both walls and roofs is added to the budget and was summed over all surfaces in the domain and divided by the number of horizontally-oriented grid points

the latent heat flux LE is zero as we did not have any green roofs in the domain. Note that the two heat fluxes are lagged to each other, with the maximum in G being reached 2 h earlier than the one for H. During the nighttime, H reaches slightly negative values around $-10\,\mathrm{W\,m^{-2}}$, indicating only limited cooling of the air during nighttime, while G becomes negative with values of less than $-30\,\mathrm{W\,m^{-2}}$, which means that a large amount of heat stored in the materials during the daytime is transferred towards the surface. The release of heat from the building materials is largely balanced by the longwave radiative cooling effect (shown implicitly by the net radiation).

The energy budget in the retrofitting scenario is qualitatively similar to that of the baseline run. However, there are two regimes of changes. A short period of time (roughly the morning hours from 0500 UTC to 1400 UTC) displays increased G values by more than $20\,\mathrm{W\,m^{-2}}$, indicating that much more energy is stored into the building envelope in the retrofitted scenario. As a result, H is decreased by $10\,\mathrm{W\,m^{-2}}$, that is, the air is not heated up as rigorously as in the baseline run. This explains why we observed a small cooling effect in the retrofitting case in the morning hours. The reason for this behavior is that the roof tiles and bitumen (or plaster in the case of walls) layer has less inertia and is decoupled from the inner roof (wall) layers by the insulation layer. It thus cools down faster in the evening, and needs to recover during the daytime.

In the second regime, which spans the period from 1400 UTC to 0500 UTC, the fluxes show the opposite differences than those in the first regime, i.e., H is larger for the retrofitting case ($10\,\mathrm{W\,m^{-2}}$), while G decreases by $20\,\mathrm{W\,m^{-2}}$. In this period, the roof tiles/bitumen (plaster for walls) layer releases its saved energy during the first regime back to the atmosphere, causing excessive warming of the air. As this regime persists much longer (15 h) than the first one (9 h), building retrofitting results in a net warming of the atmosphere over one full diurnal cycle. The warming over the course of time is also fostered by the waste heat flux from the A/C systems in office buildings. Figures 11 gives evidence that the waste heat flux sets in after three days and is then continuously increasing until the end of the simulation, thus contributing to the warming of the outdoor air. However, the average magnitude is around $3\,\mathrm{W\,m^{-2}}$ and thus much smaller than changes in the sensible heat flux. Moreover, as the nocturnal cooling effect is already getting smaller starting from the third night (cf. Fig. 7) and thus well before A/C systems are switched on, we can conclude that the waste heat flux only contributes partly to the general warming effect, which is mostly caused by the net heating from the surface in a diurnal cycle, the large-scale subsidence, and the use of cyclic boundary conditions. While the mean waste heat is relatively small, it is found to be locally on the order of $10\,\mathrm{W\,m^{-2}}$ (i.e., in the vicinity of office buildings, not shown), which explains the horizontal variability of the outdoor temperature during the early morning (see Fig. 9).

Fig. 12 shows that similar to the building surfaces, the surface energy budget for non-building surfaces reaches a quasi-stationary state shortly after model start. However, we clearly see trends in the individual fluxes: the daytime fluxes G and LE increase over the entire simulation time, while the sensible heat flux H decreases from day to day. This is directly related to the fact that boundary layer warms over time so that a) the temperature gradient and thus the sensible heat flux become smaller over time and b) more longwave radiation reaches the surface. The warmer air temperatures also provoke increased transpiration of plants to reduce their heat stress. Furthermore, we see little differences between baseline and retrofitting scenarios (not more than $\pm 5\,\mathrm{W\,m^{-2}}$). These differences are much smaller than those for the roof energy budget. Thus we conclude that the effect of building retrofitting on the energy budget of non-building surfaces is rather small and can be largely explained by the warmer air temperatures.

4. Summary

The present work aims to assess the possible effect of area-wide building retrofitting on the urban microclimate as it is currently viewed by many cities as a key strategy to reduce energy consumption and carbon emission. However, information about the retrofitting states of buildings at the city scale is usually unknown (at least for many German cities). Thus we assumed the extreme configurations of a completely non-retrofitted building scenario and a fully-retrofitted case. The results revealed that during summertime conditions, building retrofitting leads to a cooling of the urban atmosphere in the early morning hours, but a strong warming from noon to the early night hours of up to 2.5 K after one week. Interestingly, the morning cooling becomes smaller with longer simulation time and the warming effect dominates. We thus conjecture that retrofitting measures can have a severe effect on heat stress of humans and plants during long-lasting heat wave events.

The main reason for the observed behavior can be traced back to the additional insulation layer which decouples the thin plaster or roof tiles/bitumen layers for walls and roofs, respectively, on

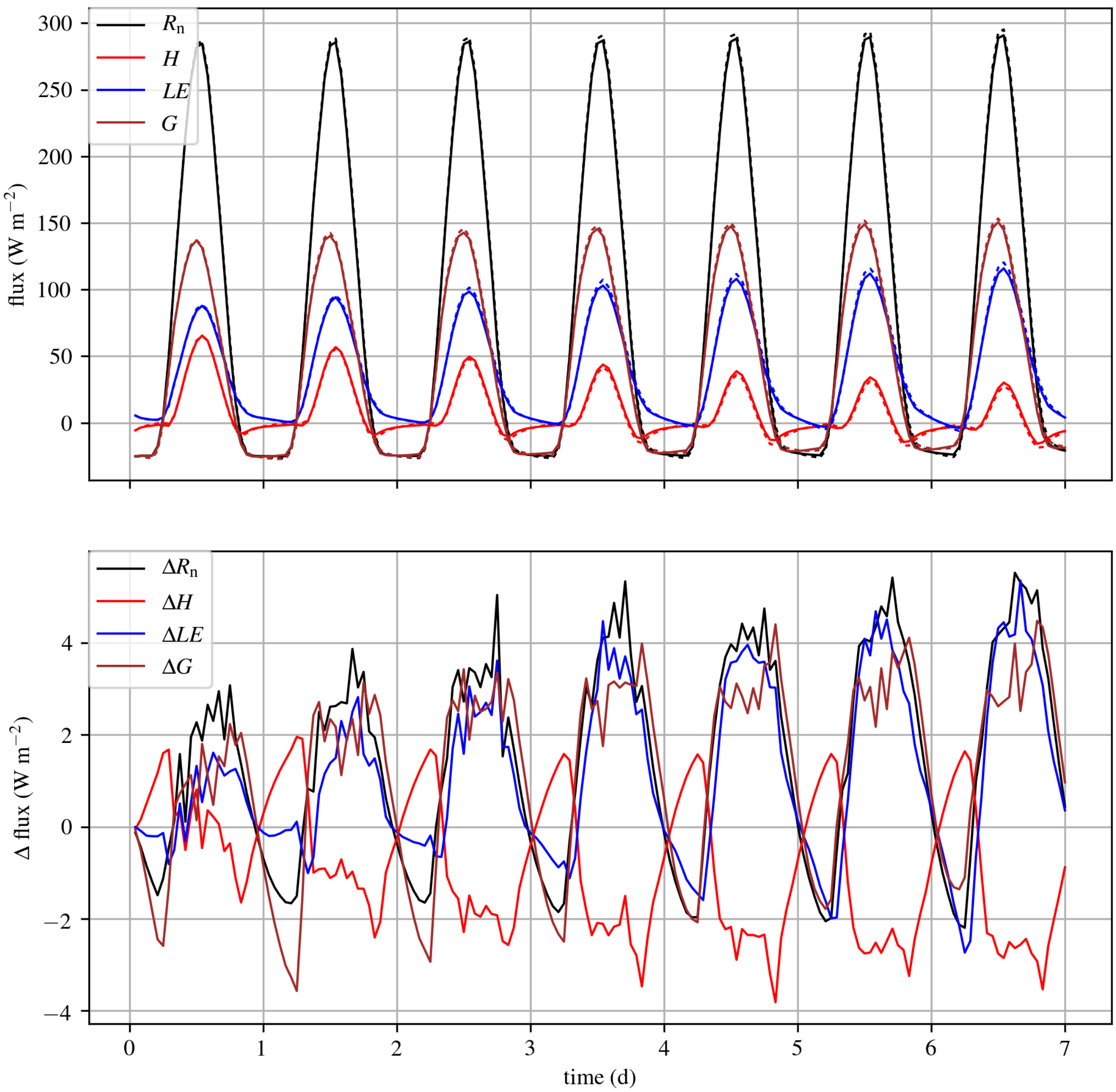

FIG. 12. As Fig. 12, but for non-building horizontal surface pixels.

top of it from the inner material layers. As a direct consequence, the top coating layer heated up more rigorously by solar irradiation, leading to higher surface temperatures and stronger heating of the air than in the baseline scenario. It also cooled down faster during nighttime, creating some cooling effects in the morning hours. We found that the net effect is a warming signal, which becomes increasingly stronger as the simulation continues. Besides, it is further strengthened by the operation of A/C systems, which results in anthropogenic waste heat released to the urban atmosphere. In our simulation this amounted to an average heating of $3\,\mathrm{W\,m^{-2}}$ after one week.

The indoor operational temperature displayed a clear tendency of remaining cooler in the retrofitting scenario (on average 4 K after one week). This indicates that building insulation can effectively reduce heat stress in indoor environments. We caution that this result was found in a one-week simulation for a mid-latitude German city which a good share of buildings being equipped with A/C systems, providing additional cooling capacities. In other climates, under longer-lasting heat waves, and with different building technologies, the situation might be different, since once the heat is inside the building, the insulation layer also acts as a trap (this is basically the desired effect in winter). The indoor environments of retrofitted buildings may take a longer time to cool down once the heat wave is over when compared to non-retrofitted buildings (if no A/C systems are installed).

As our boundary conditions were cyclic, the air was not exchanged over the simulation period, which, in conjunction with the prescribed large-scale subsidence, leads to excessively high air temperatures. In a follow-up study we will take into account fresh air supply and repeat the two simulations in order to assess whether such feedbacks are affecting the observed trend that the nocturnal cooling vanishes over time. Moreover, it would be desirable to add more runs in which a certain percent of the buildings, or a particular type of buildings, are retrofitted and a scenario without A/C systems. In that scope, future studies examining the combined effects of building retrofitting and heat mitigation strategies such as reflective roofs are encouraged. Finally, building retrofitting measures are undertaken mainly to reduce heating needs in winter. It would be of interest how building retrofitting affects the outdoor temperature and the boundary-layer growth in a winter setting. While we expect that the outdoor air temperatures would be lower due to the better building insulation, a detailed investigation is left for future work.

Acknowledgments. DL acknowledges support from the U.S. National Science Foundation (Grant ICER-1854706) and the U.S. Army Research Office (Grant W911NF-18-1-0360). Simulations were carried out on the computer clusters of the North-German Supercomputing Alliance (HLRN).

Data availability statement. The PALM model source code, set-ups, parts of the dataset on which this paper is based, as well as python scripts used for analysis and plotting are openly available at https://doi.org/10.25835/0031817. Parts of the PALM input and output data were too large to be retained or publicly archived with available resources. These data are available from Björn Maronga at Leibniz University Hannover.

APPENDIX

Building envelope configuration

TABLE A1. Building envelope configuration for status quo and retrofitting (*) simulations

Building Type	Construction	Layer (From Outside to Inside)	Thickness (m)	Thermal conductivity (W m^{-1} K^{-1})	Bulk Density (kg m^{-3})	Heat Capacity (J m^{-3} K^{-1})
Residential <1950 / Office <1950	Wall	Mortar-Plaster	0.02	0.930	1900	800
		Solid Brick	0.18	0.810	1800	840
		Solid Brick	0.18	0.810	1800	840
		Gypsum Plaster	0.02	0.700	1400	1090
	Roof	Roof Tiles	0.02	0.930	1900	800
		Wooden Formwork	0.04	0.120	415	1710
		Wooden Planks	0.02	0.120	415	1710
		Gypsum Plaster	0.02	0.700	1400	1090
	Window	Layers 1-4	0.02	0.450	2480	700
Residential 1950 - 2000 / Office 1950 - 2000	Wall	Mortar-Plaster	0.02	0.930	1900	800
		Thermal Insulation	0.06	0.046	120	660
		Concrete	0.24	2.100	2400	880
		Gypsum Plaster	0.02	0.700	1400	1090
	Roof	Bitumen	0.02	0.160	1000	1700
		Thermal Insulation	0.15	0.046	120	660
		Concrete	0.20	2.100	2400	880
		Gypsum Plaster	0.02	0.700	1400	1090
	Window	Layers 1 - 4	0.02	0.190	2480	700
Residential (*) <1950 / Office (*) <1950	Wall	Mortar-Plaster	0.02	0.930	1900	800
		Thermal Insulation	0.16	0.035	120	660
		Solid Brick	0.36	0.810	1800	840
		Gypsum Plaster	0.02	0.700	1400	1090
	Roof	Roof Tiles	0.02	0.520	1800	840
		Thermal Insulation	0.22	0.035	120	660
		Wooden Formwork & Planks	0.06	0.120	415	1710
		Gypsum Plaster	0.02	0.700	1400	1090
	Window	Layers 1 - 4	0.03	0.110	2480	700
Residential (*) 1950 - 2000 / Office (*) 1950 - 2000	Wall	Mortar-Plaster	0.02	0.930	1900	800
		Thermal Insulation	0.18	0.035	120	660
		Concrete	0.24	2.100	2400	880
		Gypsum Plaster	0.02	0.700	1400	1090
	Roof	Dry Gravel	0.02	0.520	2040	1840
		Thermal Insulation	0.24	0.035	120	660
		Concrete	0.20	2.100	2400	880
		Gypsum Plaster	0.02	0.700	1400	1090
	Window	Layers 1 - 4	0.03	0.110	2480	700

References

Ambrosini, D., G. Galli, B. Mancini, I. Nardi, and S. Sfarra, 2014: Evaluating Mitigation Effects of Urban Heat Islands in a Historical Small Center with the ENVI-met Climate Model. *Sustainability*, **6**, 7013–7029, https://doi.org/10.3390/su6107013.

Asadi, E., M. G. Da Silva, C. H. Antunes, and L. Dias, 2012: Multi-objective optimization for building retrofit strategies: A model and an application. *Energy and Buildings*, **44**, 81–87.

Best, M., and C. Grimmond, 2015: Key conclusions of the first international urban land surface model comparison project. *Bulletin of the American Meteorological Society*, **96 (5)**, 805–819.

Blocken, B., 2018: LES over RANS in building simulation for outdoor and indoor applications: A foregone conclusion? *Build. Simul.*, 1–50, https://doi.org/10.1007/s12273-018-0459-3.

BMWi, 2021: Bundesministerium für Wirtschaft und Energie: Richtlinie für die Bundesförderung für effiziente Gebäude – Einzelmaßnahmen (BEG EM), BAnz AT 07.06.2021 B2. BMWi, Bonn.

Bruse, M., and H. Fleer, 1998: Simulating surface-plant-air-interactions inside urban environments with a three dimensional numerical model. *Environ. Model. Softw.*, **13**, 373–384.

Clough, S. A., M. W. Shephard, E. J. Mlawer, J. S. Delamere, M. J. Iacono, K. Cady-Pereira, S. Boukabara, and P. D. Brown, 2005: Atmospheric radiative transfer modeling: A summary of the aer codes, short communication. *J. Quant. Spectrosc. Radiat. Transfer*, **91**, 233–244, https://doi.org/10.1016/j.jqsrt.2004.05.058.

Crank, P. J., D. J. Sailor, G. Ban-Weiss, and M. Taleghani, 2018: Evaluating the ENVI-met microscale model for suitability in analysis of targeted urban heat mitigation strategies. *Urban Climate*, **26**, 188–197, https://doi.org/10.1016/j.uclim.2018.09.002.

Deardorff, J. W., 1980: Stratocumulus-capped mixed layers derived from a three-dimensional model. *Boundary-Layer Meteorol.*, **18**, 495–527.

Deb, C., and A. Schlueter, 2021: Review of data-driven energy modelling techniques for building retrofit. *Renewable and Sustainable Energy Reviews*, **144**, 110 990.

DIN, 2013: DIN 4108-2:2013-02: Thermal protection and energy economy in buildings – Part 2: Minimum requirements to thermal insulation. Beuth Verlag GmbH, Berlin, https://doi.org/10.31030/1929159.

DIN, 2020: DIN 4108-4:2020-11: Thermal protection and energy economy in buildings – Part 4: Hygrothermal design values. Beuth Verlag GmbH, Berlin, https://doi.org/10.31030/3188939.

Früh, B., and Coauthors, 2011: Estimation of climate change impacts on the urban heat load using an urban climate model and regional climate projections. *J. Appl. Meteor. Climatol.*, **50**, 167–184.

Gehrke, K. F., M. Sühring, and B. Maronga, 2021: Modeling of land-surface interactions in the palm model system 6.0: Land surface model description, first evaluation, and sensitivity to model parameter. *Geosci. Model Dev.*, **14**, 5307–5329, https://doi.org/10.5194/gmd-14-5307-2021.

Grimmond, C. S. B., and Coauthors, 2010: The international urban energy balance models comparison project: first results from phase 1. *Journal of applied meteorology and climatology*, **49 (6)**, 1268–1292.

Grimmond, C. S. B., and Coauthors, 2011: Initial results from phase 2 of the international urban energy balance model comparison. *International Journal of Climatology*, **31 (2)**, 244–272.

Gronemeier, T., S. Raasch, and E. Ng, 2017: Effects of unstable stratification on ventilation in hong kong. *Atmosphere*, **8**, 1–15, https://doi.org/10.3390/atmos8090168.

Gronemeier, T., K. Surm, F. Harms, B. Leitl, B. Maronga, and S. Raasch, 2021: Validation of the Dynamic Core of the PALM Model System 6.0 in Urban Environments: LES and Wind-tunnel Experiments. *Geosci. Model Dev.*, **14**, 3317–3333, https://doi.org/10.5194/gmd-14-3317-2021.

Gronemeier, T., and M. Sühring, 2019: On the effects of lateral openings on courtyard ventilation and pollution – a large-eddy simulation study. *Atmosphere*, **10**, 1–23, https://doi.org/10.3390/atmos10020063.

Gross, G., 2012: Effects of different vegetation on temperature in an urban building environment. *Meteorol. Z.*, **21**, 399–412.

Gross, G., 2017: Some effects of water bodies on the environment – numerical experiments. *J. Heat Island Inst. Int.*, **12**, 1–11.

Günther, R., 2014: The role of soil water content for microclimatic effects of green roofs and urban trees – a case study from Berlin, Germany. *J. Heat Island Inst. Int.*, **9**, 19–25.

Hagishima, A., J. Tanimoto, and K.-i. Narita, 2005: Intercomparisons of experimental convective heat transfer coefficients and mass transfer coefficients of urban surfaces. *Boundary-Layer Meteorology*, **117 (3)**, 551–576.

Heldens, W., C. Burmeister, F. Kanani-Sühring, B. Maronga, D. Pavlik, M. Sühring, J. Zeidler, and T. Esch, 2020: Geospatial input data for the palm model system 6.0: model requirements, data sources and processing. *Geosci. Model Dev.*, **13**, 5833–5873, https://doi.org/10.5194/gmd-13-5833-2020.

Inagaki, A., M. Castillo, Y. Yamashita, M. Kanda, and H. Takimoto, 2011: Large-eddy simulation of coherent flow structures within a cubical canopy. *Boundary-Layer Meteorol.*, **142**, 207–222.

Krayenhoff, E. S., and J. A. Voogt, 2007: A microscale three-dimensional urban energy balance model for studying surface temperatures. *Boundary-Layer Meteorol.*, **123**, 433–461, https://doi.org/10.1007/s10546-006-9153-6.

Krayenhoff, E. S., and Coauthors, 2021: Cooling hot cities: a systematic and critical review of the numerical modelling literature. *Environ. Res. Lett.*, **16**, 053 007, https://doi.org//10.1088/1748-9326/abdcf1.

Krč, P., J. Resler, M. Sühring, S. Schubert, M. H. Salim, and V. Fuka, 2021: Radiative transfer model 3.0 integrated into the palm model system 6.0. *Geosci. Model Dev.*, **14**, 3095–3120, https://doi.org/10.5194/gmd-14-3095-2021.

Kurrpa, M., and Coauthors, 2020: Sensitivity of spatial aerosol particle distributions to the boundary conditions in the palm model system 6.0. *Geosci. Model Dev.*, **13**, 5663–5685.

Letzel, M. O., C. Helmke, E. Ng, X. An, A. Lai, and S. Raasch, 2012: Les case study on pedestrian level ventilation in two neighbourhoods in hong kong. *Meteorol. Z.*, **21**, 575–589.

Letzel, M. O., M. Krane, and S. Raasch, 2008: High resolution urban large-eddy simulation studies from street canyon to neighbourhood scale. *Atmos. Env.*, **42**, 8770–8784.

Li, D., E. Bou-Zeid, and M. Oppenheimer, 2014: The effectiveness of cool and green roofs as urban heat island mitigation strategies. *Environmental Research Letters*, **9 (5)**, 055 002.

Loga, T., B. Stein, N. Diefenbach, and R. Born, 2015: Deutsche Wohngebäudetypologie - Beispielhafte Maßnahmen zur Verbesserung der Energieeffizienz von typischen Wohngebäuden. Institut Wohnen und Umwelt GmbH.

Maronga, B., and Coauthors, 2015: The parallelized large-eddy simulation model (PALM) version 4.0 for atmospheric and oceanic flows: Model formulation, recent developments, and future perspectives. *Geosci. Model Dev.*, **8**, 2515–2551, https://doi.org/10.5194/gmd-8-2515-2015.

Maronga, B., and Coauthors, 2020: Overview of the PALM model system 6.0. *Geosci. Model. Dev.*, **13**, 1335–1372, https://doi.org/10.5194/gmd-2019-103.

Oke, T. R., G. Mills, A. Christen, and J. A. Voogt, 2017: *Urban Climates*. Cambridge, https://doi.org/10.1017/9781139016476.

Ortiz, M., L. Itard, and P. M. Bluyssen, 2020: Indoor environmental quality related risk factors with energy-efficient retrofitting of housing: A literature review. *Energy and Buildings*, **221**, 110 102.

Pfafferott, J., S. Rißmann, M. Sühring, F. Kanani-Sühring, and B. Maronga, 2021: Building indoor model in palm model system 6.0: Indoor climate, energy demand, and the interaction between buildings and the urban climate. *Geosci. Model Dev.*, **14**, 3511–3519, https://doi.org/10.5194/gmd-14-3511-2021.

Rabani, M., H. B. Madessa, and N. Nord, 2017: A state-of-art review of retrofit interventions in buildings towards nearly zero energy level. *Energy procedia*, **134**, 317–326.

Resler, J., and Coauthors, 2017: PALM-USM v1.0: A new urban surface model integrated into the PALM large-eddy simulation model. *Geosci. Model Dev.*, **10**, 3635–3659, https://doi.org/10.5194/gmd-10-3635-2017.

Resler, J., and Coauthors, 2021: Validation of the palm model system 6.0 in real urban environment; case study of prague-dejvice, czech republic. *Geosci. Model Dev.*, **14**, 4797–4842, https://doi.org/10.5194/gmd-14-4797-2021.

Rosenzweig, C., W. Solecki, S. A. Hammer, and S. Mehrotra, 2010: Cities lead the way in climate–change action. *Nature*, **467 (7318)**, 909–911.

Saiki, E. M., C.-H. Moeng, and P. P. Sullivan, 2000: Large-eddy simulation of the stably stratified planetary boundary layer. *Boundary Layer Meteorol.*, **95**, 1–30.

Salim, M. H., K. H. Schlünzen, D. Grawe, M. Boettcher, A. M. U. Gierisch, and B. Fock, 2018: The Microscale Obstacle Resolving Meteorological Model MITRAS: Model Theory. *Geosci. Model Dev. Discuss.*, https://doi.org/10.5194/gmd-2017-250.

Salim, M. H., S. Schubert, J. Resler, P. Krč, B. Maronga, F. Kanani-Sühring, M. Sühring, and C. Schneider, 2020: Importance of radiative transfer processes in urban climate models: A study based on the palm model system 6.0. *Geosci. Model Dev. Discuss.*, https://doi.org/10.5194/gmd-2020-94, preprint.

Schlünzen, K. H., and Coauthors, 2003: Flow and Transport in the Obstacle layer: First Results of the Micro-Scale Model MITRAS. *J. Atmos. Chem.*, **44**, 113–130.

Sinsel, T., H. Simon, A. M. Broadbent, M. Bruse, and J. Heusinger, 2021: Modeling the ourdoor cooling impact of highly radiative "super cool materials". *Urban Climate*, **38**, 100 898, https://doi.org/10.1016/j.uclim.2021.100898.

Theeuwes, N. E., G.-J. Steeneveld, R. J. Ronda, M. W. Rotach, and A. A. Holtslag, 2015: Cool city mornings by urban heat. *Environmental Research Letters*, **10 (11)**, 114 022.

United Nations, 2016: The World's Cities in 2016 - Data Booklet. Tech. Rep. ST/ESA/SER.A/392, United Nations, Department of Economic and Social Affairs.

Wang, L., M. Huang, and D. Li, 2020: Where are white roofs more effective in cooling the surface? *Geophysical Research Letters*, **47 (15)**, e2020GL087 853.

Wang, L., M. Huang, and D. Li, 2021: Strong influence of convective heat transfer efficiency on the cooling benefits of green roof irrigation. *Environmental Research Letters*, **16 (8)**, 084 062.

Wicker, L. J., and W. C. Skamarock, 2002: Time-splitting methods for elastic models using forward time schemes. *Mon. Wea. Rev.*, **130**, 2088–2097.

Williamson, J. H., 1980: Low-storage runge-kutta schemes. *J. Comput. Phys.*, **35**, 48–56.

Yaghoobian, N., J. Kleissl, and K. T. Paw U, 2014: An improved three-dimensional simulation of the diurnally varying street-canyon flow. *Boundary-Layer Meteorol.*, DOI:10.1007/s10546-014-9940-4.